

Modelling of Wideband Concentric Ring Frequency Selective Surface for 5G Devices

Ankush Kapoor¹, Pradeep Kumar^{2,*} and Ranjan Mishra³

¹Department of Electronics and Communication Engineering, Jawaharlal Nehru Government Engineering College, Sundernagar, 175018, India

²Discipline of Electrical, Electronic and Computer Engineering, University of KwaZulu-Natal, Durban, 4041, South Africa

³Department of Electrical and Electronics Engineering, University of Petroleum and Energy Studies, Dehradun, 248007, India

*Corresponding Author: Pradeep Kumar. Email: pkumar_123@yahoo.com

Received: 21 February 2022; Accepted: 20 May 2022

Abstract: Frequency selective surfaces (FSSs) play an important role in wireless systems as these can be used as filters, in isolating the unwanted radiation, in microstrip patch antennas for improving the performance of these antennas and in other 5G applications. The analysis and design of the double concentric ring frequency selective surface (DCRFSS) is presented in this research. In the sub-6 GHz 5G FR1 spectrum, a computational synthesis technique for creating DCRFSS based spatial filters is proposed. The analytical tools presented in this study can be used to gain a better understanding of filtering processes and for constructing the spatial filters. Variation of the loop sizes, angles of incidence, and polarization of the concentric rings are the factors which influence the transmission coefficient as per the thorough investigation performed in this paper. A novel synthesis approach based on mathematical equations that may be used to determine the physical parameters of DCRFSS-based spatial filters is presented. The proposed synthesis technique is validated by comparing results from high frequency structure simulator (HFSS), Ansys electronic desktop circuit editor, and an experimental setup. Furthermore, the findings acquired from a unit cell are expanded to a 2×2 array, which shows identical performance and therefore proves its stability.

Keywords: Spatial filters; double concentric ring frequency selective surface (DCRFSS); angle of incidence; finite element method (FEM); polarization angles

1 Introduction

Wireless systems are protected by spatial domain selection algorithms against unwanted signals sent by other communication equipment, which can create interference. These filters include a built-in frequency selection that improves the radiation performance of a radiator. Frequency selective surfaces (FSS) have attracted a lot of attention in recent years as a method of constructing spatial filters because



This work is licensed under a Creative Commons Attribution 4.0 International License, which permits unrestricted use, distribution, and reproduction in any medium, provided the original work is properly cited.

they may impart filtering features in the spatial domain [1–5]. Recent study has sought to build and promote a square shaped loop, circumferential ring, ellipsoid, hexagonal geometry, and a cross dipole as geometric patterns that might be employed in the electromagnetic spectrum [6–8]. These filters are used in telecommunications to control electromagnetic radiation. They can, nevertheless, be used for weighing in other fields, such as high-gain antenna sub-reflectors, material processing, and dielectric electromagnetic shielding [9–11]. After looking at the conductive square loops [12], a mathematical analysis was undertaken, and an analogous geometrical shape was given. The behavior of the FSS is investigated using a unit cell from an array. As a result, selecting the proper unit cell shape is crucial for ensuring that the planned structure operates at the desired frequency. The architectural design, patch/slot geometry, spacing between components, and superstrate material are all key aspects in determining crucial FSS features such resonance frequency, bandwidth, and Q-factor [13]. FSS may be employed for energy harvesting and electromagnetic shielding [14–19], as well as for the optimization of the electromagnetic coupling and further providing angular stability with shrinking of unit cells. Multiple layers cascaded together in the FSS design for sub-6 GHz proposed has the downside of increasing overall thickness and complexity [20,21]. Circular frequency selective surface shape is widely used in the upper microwave spectrum for a variety of purposes. A simple synthesis approach for assessing the DCRFSS, which was utilized to construct the structure at 3 GHz, 15 GHz, and 26 GHz resonating frequencies, is described in [22]. The Jerusalem cross FSS complementing structures are devised, which offers efficient electromagnetic shielding in the X-band of the microwave frequency spectrum [23]. Due to their symmetrical geometry, the square loop and concentric circular ring are less sensitive to changes in angle of incidence (AOI) than other shaped structures [24–26]. As detailed in the literature [27–29], the architecture of FSS is represented by an analogous circuit model that aids in the extraction of their electrical properties. The launch of the sub-6-GHz 5G cell spectrum frequency is based on optimizing the existing 4G technology that the industry has previously created. Sub-6 GHz is a turning point in terms of coverage and penetration, and the 5G experience is vastly different from that of mm-wave [30–33]. A novel synthesis approach based on mathematical equations is used to determine the physical parameters of DCRFSS-based spatial filters. The development of a periodic unit cell structure with double concentric ring frequency selective surface (DCRFSS) with band-pass behavior in the sub-6 GHz 5G spectrum is discussed by using a numerical synthesis technique. The synthesis is based on a basic equivalent circuit model analysis approach that allows for massive computations in a short period of time. The lumped circuit characteristics are obtained by using the equivalent circuit modelling (ECM) approach. The simulations are run on the Ansys HFSS simulator, which is based on the finite element method (FEM). The achievements are assessed in terms of providing modelled geometry and a synthesis technique for measuring and estimating the dimensions of the DCRFSS structure. To guarantee that the transmission and reflection coefficients are accurate, the prototype is created and tested. The manuscript is structured around the design of the double concentric ring FSS along with the mathematical analysis which is presented in the Section 2. In part 3, the outcomes are derived from theoretical notions are contrasted to the simulated results. The study is expanded to formation of an array in part 4, and the findings are provided for the DCRFSS structure, with a closing comment in the Section 5.

2 Structure

This section outlines the architectural design of the DCRFSS. By using the mathematical formulas provided by Marcuvitz [34] for conductive strips, an efficient approach employing equivalent circuit model (ECM) is applied to examine the intended shape. The equivalent circuit approach is more efficient to employ when paired with computational optimization techniques because of the ease of the

attempts substituted for the realization with little computational effort. The angle of incidence (AOI) is a critical metric that must be considered while determining design specifications. The technique for evaluating periodic gratings proposed by Marcuvitz has been initially tested on square loop FSS structures [35–37]. In addition, a correction term was included in [38] to eliminate the inaccuracy of this technique for oblique angles of incidence. Due to its simplicity and ability to drastically save time and computational effort when compared to the full wave technique, equivalent circuit model (ECM) analysis and construction of an FSS is an easily accepted solution. It also gives the proposed structure a clear electromagnetic comprehension. The resonant frequencies may be calculated by using principle of the LC circuits which are demonstrated in the Eqs. (1) and (2) as shown below:

$$f_{r1} = \frac{1}{2\pi\sqrt{L_1C_1}} \quad (1)$$

$$f_{r2} = \frac{1}{2\pi\sqrt{L_2C_2}} \quad (2)$$

where f_{r1} and f_{r2} are the resonance frequencies of each ring construction, and L_1 , C_1 , L_2 & C_2 are the inductance and capacitance values associated with each concentric ring. At the resonance frequencies, the FSS achieves maximum current distribution, resulting in a transmission null as all incident power is radiated back. Marcuvitz [34], who devised formulae for deriving estimated values of inductances and capacitances of periodic conductive strips, is credited with the foundation of the ECM approach. The inductive impedances and capacitive susceptibility values are defined as follows:

$$\frac{\omega_r L}{Z_0} = \frac{1}{p} \cos \theta * F(p, t, \lambda, \theta) \quad (3)$$

$$F(p, t, \lambda, \theta) = \frac{p'}{\lambda} \left[\ln \csc \left(\frac{\pi t}{2p} \right) + G(p, t, \lambda, \theta) \right] \quad (4)$$

$$\frac{\omega_r C}{Y_0} = 4 \frac{1}{p} \sec \phi * F(p, g, \lambda, \phi) * \epsilon_{\text{eff}} \quad (5)$$

where ϵ_{eff} is the effective permittivity of the surface.

$$F(p, g, \lambda, \phi) = \frac{p}{\lambda} \left[\ln \csc \left(\frac{\pi g}{2p} \right) + G(p, g, \lambda, \phi) \right] \quad (6)$$

where p' and t' depicts the value of the periodicity and thickness of the conductive ring respectively; θ and ϕ represents the incidence angles; λ denotes the wavelength of incident radiations; and $G(\cdot)$ denotes a function for incorporating a correction term (CT). The parameters of the DCRFSS structure, such as the circumference of the ring (d), unit cell periodicity (p), and thickness of the metal conductor, are used to extract lumped circuit components such as inductance and capacitance (t), gap between the adjacent rings (g), angle of incidence (θ for TE and ϕ for TM) and the wavelength of the incident ray (λ) by using equivalent circuit model analysis approach. In the Fig. 1, a copper sheet (dark blue color) with thickness (t_c) of 0.002 cm and conductivity (σ) of 5.8×10^7 S/m is engraved and deposited over the Flame Retardant 4 (FR4) dielectric substrate.

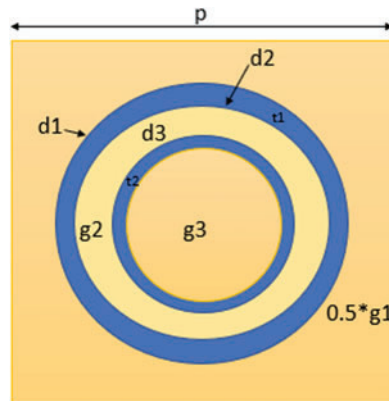


Figure 1: Schematic of DCRFSS unit cell

However, to achieve resonance at the necessary frequencies with the desired bandwidth, it is advisable to define the parameters together with the periodicity for the circular ring in the creation of DCRFSS structure. In the literature, [19] and [22] provide an effective synthesis procedure that allowed us to create a precise mathematical analysis by utilizing the ECM approach. The electrons on the metallic sheet vibrate when the incidence plane wave contacts the surface of the metallic patches. When the electric field is parallel to the surface of the metallic strip, an inductive component emerges; when it is perpendicular to the plane of the metallic strip, a capacitive component emerges. Using this method, an equivalent circuit can be constructed for the FSS which can show low, high, band-pass, or band-stop filter behavior depending on the chosen shape. In the case of the circular ring FSS, the diameter and periodicity of the structure must be determined to calculate the resonant frequency of operation. The meta-analysis presented only provides the information about the values of inductance (L) and capacitance (C) for a circular ring structure but analyzing the geometrical relationship of lumped circuit elements with the model parameters at the specified resonance frequency is a difficult task. The analysis is expanded to the construction of a new equivalent circuit for the suggested concentric ring circular aperture, as shown in the Fig. 2b, and an array depiction of 2×2 cells is shown in the Fig. 2a.

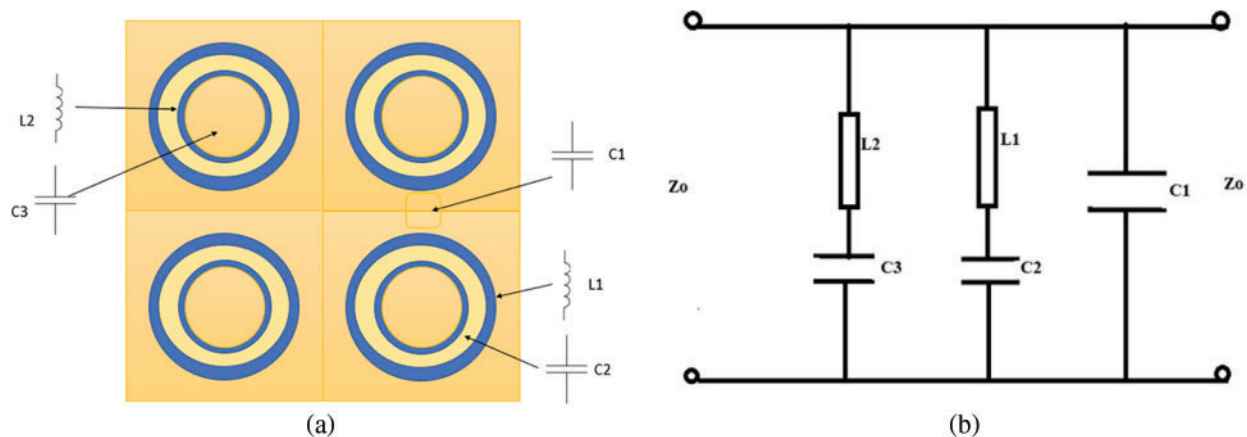


Figure 2: DCRFSS array illustrating (a) 2×2 array, (b) equivalent circuit of a unit cell

Fig. 2b depicts the suggested equivalent circuit, which consists of a capacitive branch (C1) that represents the gap between two outer neighboring rings. The branch (C2-L1) represents the reactance's associated with copper conductor of the outer ring and the gap between the two concentric rings apertures. The branch (C3-L2) represents the interactions between the inner concentric ring and the gap lying within the ring. The lumped circuit elements are extracted by using the equations which are given by:

$$\frac{B_{C_1}}{Y_0} = 4 \sec(\phi) F(p, d_1 - 2CT, \lambda, \phi) \quad (7)$$

$$\frac{X_{L_1}}{Z_0} = \frac{1}{\epsilon_{\text{eff}}} \left[\left(\frac{X_{L1\text{int}}}{Z_0} \right) + \left(\frac{X_{L1\text{int}2}}{Z_0} \right) \right] \quad (8)$$

$$\frac{X_{L_2}}{Z_0} = \frac{1}{\epsilon_{\text{eff}}} \left[\left(\frac{X_{L1\text{int}2}}{Z_0} \right) + \left(\frac{X_{L2\text{int}}}{Z_0} \right) \right] \quad (9)$$

$$\frac{B_{C_2}}{Y_0} = \left(\frac{B_{C2\text{int}}}{Y_0} \right) + \frac{d_3 + g_2 + 2CT}{t_1} \left(\frac{B_{C_1}}{Y_0} \right) \quad (10)$$

$$\frac{B_{C_3}}{Y_0} = (10) \left(\frac{B_{C3\text{int}}}{Y_0} \right) + \frac{d_3 - 2t_2 + g_3 + 2CT}{t_1} \left(\frac{B_{C3\text{int}}}{Y_0} \right) \quad (11)$$

$$\text{where } \left(\frac{B_{C2\text{int}}}{Y_0} \right) = \frac{p}{\pi \left(\frac{d_2}{2} \right)} F(p, 2t_2, \lambda, \phi) \quad (12)$$

$$\left(\frac{B_{C3\text{int}}}{Y_0} \right) = \left(\frac{2}{\pi} \right) \left(\frac{p}{d_3 - 2t_2} \right) F(p, d_3 - 2t_2, \lambda, \phi) \quad (13)$$

$$\left(\frac{X_{L1\text{int}}}{Z_0} \right) = F(p, d_1 - 2CT, \lambda, \theta) \quad (14)$$

$$\left(\frac{X_{L1\text{int}2}}{Z_0} \right) = F(d_1 - t_1, t_1, \lambda, \theta) \quad (15)$$

$$\left(\frac{X_{L2\text{int}}}{Z_0} \right) = 2F(d_3 - t_2, t_2, \lambda, \theta) \quad (16)$$

The series of Eq. (7) up to Eq. (15) gives the inductive and the capacitive behaviors of the ring apertures for the designed geometry. The value of C_1 is evaluated by the Eq. (7). The value of C_2 is extracted by the interaction of inner ring aperture of effective thickness t_2 and the outer ring aperture of thickness t_1 and the gap between the two rings as g_2 as illustrated in Eq. (10). Further, the value of C_3 is evaluated in the Eq. (11) and contains the numeric value attained by the capacitive reactance of the inner circular ring (multiplied by an amplification factor of 10 due to its high influence). In the Eq. (8), the value of L_1 is computed considering the inductance offered by outer conductive loop. For the value of L_2 , the Eq. (9) is used for calculating inductive impedance offered by inner concentric ring. The subscript int is used to indicate an intermediate variable for obtaining the final parameter. It is

important to define the added term CT which denotes the correction term and is related to the average value of g_r , in accordance with the diameter chosen for making the conductive ring and is given as:

$$CT = \frac{\int_{-\frac{d}{2}}^{\frac{d}{2}} \left| \left(\frac{d}{2} \right) - \sqrt{\left(\frac{d}{2} \right)^2 - x^2} \right| dx}{d} \quad (17)$$

The Eq. (17) gives the correction term average value which is related to the diameter of the ring and it has proven to be an interesting approach in providing accurate results of the proposed ECM. In Eqs. (8) and (9), the term used ϵ_{eff} denotes the values of effective relative permittivity of the dielectric substrate explained in [35] and given as:

$$\epsilon_{\text{eff}} = \epsilon_r + (\epsilon_r - 1) \left(\frac{-1}{e^{MN}} \right) \quad (18)$$

where $M = 10h'/p'$ in which h' signifies the effective thickness of the substrate, ϵ_r represents the relative permittivity and the constant term N is dependent on the geometry and is related to the amount of conductive element present in the geometry [37]. The value of N is obtained according to the methodology given by [39] for different geometries. On generalizing the Eq. (18), the expression reduces to:

$$\epsilon_{\text{eff}} = \frac{\epsilon_1 + \epsilon_2}{2}; \text{ for } h \sim 0.02\lambda_0 \quad (19)$$

In the above equation ϵ_1 takes the value of ϵ_r for the FR4 substrate i.e., 4.4 and ϵ_2 is substituted with the dielectric permittivity of the air which has the value of unity. The dimensions of the parameters such as thickness of the ring (t) are calculated for different values of (t/λ) and the periodicity (p) is evaluated by using grating lobe condition given by:

$$p(1 + \sin \theta) < \frac{\lambda}{\sqrt{\epsilon_{\text{eff}}}} \quad (20)$$

It has been stated that a generalized equation for linking the aforementioned parameters can be derived after additional simplification.

$$p = M\lambda \quad (21)$$

where M denotes the constant of proportionality whose values lies in between 0 and 1. Considering the modal analysis of thin concentric rings dispersed periodically along any two skewed coordinates are revealed with an incident plane wave of any polarization striking at any of the oblique angles, as seen in the Fig. 3. It is important to get noted that the spacing between the ring elements should always be less than or equal to $\lambda/2$.

As demonstrated in the Fig. 3, a plane wave with propagation vector k strikes an array of rings which are distributed along the skewed coordinates s_1 and s_2 respectively. The distribution of the rings is such that the angle between k and the normal to the surface is denoted by θ and the angle between projection vector s_1 and k is given by ϕ . The positioning of the electromagnetic fields in the vicinity of the array of FSS must meet the Floquet theorem's periodicity criterion. The scalar wave equation by using the Floquet's theorem is given by [40]:

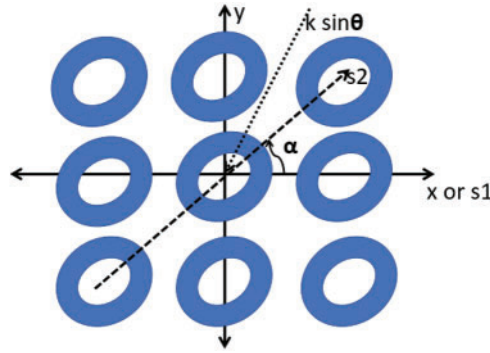


Figure 3: Geometrical placement of circular ring FSS

$$\psi_{mn} = e^{-j(U_{mn}x + V_{mn}y + W_{mn}z)} \tag{22}$$

where $U_{mn} = k \sin \theta \cos \Phi + \frac{2\pi m}{dx}$ (23)

$$V_{mn} = k \sin \theta \cos \Phi + \frac{2\pi n}{dy} - \frac{2\pi m}{dx \tan \alpha} \tag{24}$$

$$W_{mn} = \begin{cases} \sqrt{k^2 - T_{mn}^2} & \text{for } k^2 > T_{mn}^2 \\ -j\sqrt{T_{mn}^2 - k^2} & \text{for } T_{mn}^2 > k^2 \end{cases} \tag{25}$$

and the term T_{mn}^2 is given by:

$$T_{mn}^2 = U_{mn}^2 + V_{mn}^2 \tag{26}$$

In the above equations, m and n denotes the Floquet indices. The term W_{mn} indicates the propagation constants of the incident rays which attain positive values for propagating modes and exhibits negative imaginary values for evanescent modes. The components pertaining to the electric field distribution which are transverse to the z axis can be expressed in terms of the factor ψ as given below:

$$\Delta_{mn \text{ TE}} = \frac{1}{\sqrt{dx \, dy}} \left(\frac{V_{mn}}{T_{mn}} \dot{x} - \frac{U_{mn}}{T_{mn}} \dot{y} \right) \psi_{mn \text{ TE modes}} \tag{27}$$

$$\Delta_{mn \text{ TM}} = \frac{1}{\sqrt{dx \, dy}} \left(\frac{U_{mn}}{T_{mn}} \dot{x} + \frac{V_{mn}}{T_{mn}} \dot{y} \right) \psi_{mn \text{ TM modes}} \tag{28}$$

The above mentioned fields are related to each other as given below:

$$\eta_{mn \text{ TE}} = \frac{k\eta_0}{W_{pq}} \tag{29}$$

$$\eta_{mn \text{ TM}} = \frac{W_{pq}\eta_0}{k} \tag{30}$$

The incident plane wave consisting of unit intensity electric field propagating in the direction of (θ, ϕ) , can be expressed by the addition of the E and H polarized plane waves. The incident plane waves correspond to the TE and TM Floquet modes consisting of values $m, n=0$. Hence, the values of the incident electric and magnetic fields:

$$\dot{\mathbf{E}}^i = \sum_{r=1}^2 A_{00r} \Delta_{00r} \quad (31)$$

$$\dot{\mathbf{H}}^i = \sum_{r=1}^2 \frac{A_{00r}}{\Delta_{00r}} (\hat{\mathbf{z}} \times \Delta_{00r}) \quad (32)$$

In the above expressions, the term r denotes the TE and TM modes. The factor A_{00r} denotes the magnitude of the component. The scattered fields can be expressed in terms of the reflection coefficient R_{mnr} as given below:

$$\dot{\mathbf{E}}^s = \sum_m \sum_n \sum_{r=1}^2 R_{mnr} \Delta_{mnr} \quad (33)$$

$$\dot{\mathbf{H}}^s = - \sum_m \sum_n \sum_{r=1}^2 \frac{R_{mnr}}{\eta_{mnr}} (\hat{\mathbf{z}} \times \Delta_{mnr}) \quad (34)$$

The value of the unknown reflection coefficient R_{mnr} is given by:

$$R_{mnr} = \eta_{mnr} \iint \hat{\mathbf{z}} \times \dot{\mathbf{H}}^s \cdot \Delta_{mnr}^* da \quad (35)$$

The analysis of the electromagnetic behavior of the circular ring is completed by signifying the boundary conditions which are given by:

$$\dot{\mathbf{E}}^s + \dot{\mathbf{E}}^i = 0 \text{ for each loop} \quad (36)$$

$$(\dot{\mathbf{H}}^s + \dot{\mathbf{H}}^i) 2\hat{\mathbf{z}} = \hat{\mathbf{K}} \quad (37)$$

Now, substituting the Eq. (35) in Eq. (33) and incorporating the values of Eqs. (31) and (33) into the Eq. (36) we get:

$$\sum_{r=1}^2 A_{00r} \Delta_{00r} = - \sum_m \sum_n \sum_{r=1}^2 \eta_{mnr} \Delta_{mnr} \iint \hat{\mathbf{z}} \times \dot{\mathbf{H}}^s \cdot \Delta_{mnr}^* da \quad (38)$$

For simplification of the Eq. (38), the induced current, $-\hat{\mathbf{z}} \times \dot{\mathbf{H}}^s$ is replaced by another set of orthonormal mode functions which are compatible to the geometry of circular rings and also satisfy boundary conditions as shown below:

$$-\hat{\mathbf{z}} \times \dot{\mathbf{H}}^s = \sum_m \sum_n \sum_{l=1}^2 (\mathbf{B}_{mnl} \psi_{mnl}) + \mathbf{B}_{\text{TEM}} \psi_{\text{TEM}} \quad (39)$$

The limits for the mode coefficients ranges from $l = 1$ to $l = 2$ which denotes TE and TM modes respectively. The terms ψ_{mnl} and ψ_{TEM} for circular rings can be expressed as [41]:

$$\psi_{mn}^{TE} = \check{\rho} \frac{n}{\rho} Z_n(k'_{cmn} \rho) \sin n\phi + \check{\phi} k'_{cmn} Z'_n(k'_{cmn} \rho) \cos n\phi \tag{40}$$

$$\psi_{mn}^{TM} = \check{\rho} k_{cmn} \check{Z}'_n(k_{cmn} \rho) \sin n\phi + \check{\phi} \frac{n}{\rho} \check{Z}_n(k_{cmn} \rho) \cos n\phi \tag{41}$$

$$\psi_{TEM} = \frac{1}{\rho \ln \frac{b}{a}} [\check{x} \cos n\phi + \check{y} \sin n\phi] \tag{42}$$

where the simplified terms Z_n and \check{Z}_n are given by:

$$Z_n = \frac{\sqrt{\pi \epsilon_n}}{2 \sqrt{\left(\frac{J_n(k'_{cmn} b)}{J_n(k'_{cmn} a)}\right)^2 \left(1 - \left(\frac{n}{a}\right)^2\right) - \left(1 - \left(\frac{n}{b}\right)^2\right)}} \times (Y'_n(k'_{cmn} a) J_n(k'_{cmn} \rho) - J'_n(k'_{cmn} a) Y_n(k'_{cmn} \rho)) \tag{43}$$

$$\check{Z}_n = \frac{\sqrt{\pi \epsilon_n}}{2 \sqrt{\left(\frac{J_n(k_{cmn} b)}{J_n(k_{cmn} a)}\right) - 1}} \times (Y_n(k_{cmn} a) J_n(k_{cmn} \rho) - J_n(k_{cmn} a) Y_n(k_{cmn} \rho)) \tag{44}$$

where the terms k_{cmn} and k'_{cmn} is the m^{th} root of the equations as given below :

$$\left(Y'_n(k'_c) J'_n\left(k'_c \frac{b}{a}\right) - J'_n(k'_c) Y'_n\left(k'_c \frac{b}{a}\right) \right) = 0 \quad \forall k'_{cmn} \tag{45}$$

$$\left(Y_n(k_c) J_n\left(k_c \frac{b}{a}\right) - J_n(k_c) Y_n\left(k_c \frac{b}{a}\right) \right) = 0 \quad \forall k_{cmn} \tag{46}$$

On multiplying, both sides of the Eq. (39) by the complex conjugate of the coefficients ψ_{mnl} and ψ_{TEM} and integrating the finalized product value over the circular ring, the results are retrieved as [38]:

$$\sum_{r=1}^2 A_{00r} C_{00r}^{*TEM} = - \sum_m \sum_n \sum_{r=1}^2 \eta_{mnr} C_{mnr}^{*TEM} \iint \dot{z} \times \dot{H}^s \cdot \Delta_{mnr}^* da \tag{47}$$

$$\sum_{r=1}^2 A_{00r} C_{00r}^{*ABL} = - \sum_m \sum_n \sum_{r=1}^2 \eta_{mnr} C_{mnr}^{*ABL} \iint \dot{z} \times \dot{H}^s \cdot \Delta_{mnr}^* da \tag{48}$$

where the coefficient terms C_{mnr}^{*TEM} and C_{mnr}^{*ABL} are given by:

$$C_{mnr}^{*ABL} = \iint \psi_{ABL} \cdot \Delta_{mnr}^* da \tag{49}$$

$$C_{mnr}^{*TEM} = \iint \psi_{TEM} \cdot \Delta_{mnr}^* da \tag{50}$$

Hence, the integral equation can be generalized into:

$$[Z_{MNL}^{mnl}] [B_{mnl}] = [D_{mnl}] \tag{51}$$

where Z denotes the square matrix in which the row index is designated by M,N,L and the column matrix is designated by m,n,l. The unknown coefficients B_{mnl} and B_{TEM} must be evaluated from the Eq. (51) and substituted in the Eq. (40) for evaluation of the reflection coefficient R_{mnr} , as suggested in [7].

3 Parametric Variations

The synthesis technique is validated by presenting a diagnosis as described. The physical measurements of the concentric circular ring based FSS spatial filter to be used in operation from 3 to 4.5 GHz are accessed by using the architecture equations. The Eqs. (6) to (15) are utilized for calculating the lumped circuit elements of the ECM from the parameters of the physical model and the reflection coefficient is predicted by using the Eqs. (22) to (35). In addition to the mathematical calculations, the results retrieved are validated by conducting simulations in the ANSYS tools of HFSS v20 and the ECM is performed on Electronic Desktop Circuit Editor. After the validation of the ECM, the design is authenticated by reporting the measurement results of the designed prototype. Theoretical research and existing studies indicate that, because to its symmetrical construction, DCRFSS provides the optimum performance; nevertheless, when the incidence angle of the wave striking it varies, its properties alter substantially after a certain angle. The FSS unit cell was examined at 0° in the first step, deriving its dimensions according to Tab. 1.

Table 1: Unit cell dimensions of DCRFSS

Parameters	Values
f_{r1}	3.13 GHz
f_{r2}	5.18 GHz
p	$0.55 \lambda_{mid}$
t_1	$0.0069 \lambda_{mid}$
t_2	$0.013 \lambda_{mid}$
d_1	$0.207 \lambda_{mid}$
d_2	$0.20 \lambda_{mid}$
d_3	$0.09 \lambda_{mid}$

where the terms f_{r1} denote the lower resonant frequency, f_{r2} signifies the higher resonant frequency, λ_{mid} denotes the centre operating frequency wavelength, p denote the periodicity of DCRFSS structure, d_1 is the diameter of the outer part of external ring, d_2 is the diameter of the inner part of external ring and d_3 is the diameter of the outer part of internal ring, t_1 is the effective thickness of the outer ring of DCRFSS and t_2 is the effective thickness of the inner ring of DCRFSS. The band pass behaviour of the DCRFSS is illustrated in the Fig. 4. To retrieve its value at the appropriate resonant frequencies of activity without ignoring the grating lobes, the Eq. (19) must be satisfied. Thus, for normal angle of incidence, Eq. (19) reduces to:

$$p < \frac{\lambda}{\sqrt{\epsilon_{eff}}}; p < \lambda \text{ for } \sqrt{\epsilon_{eff}} \approx 1; \quad (52)$$

Also, a dedicated expression for the outer ring conductor is extracted from the Eq. (20) in the sub-6 GHz band as given below:

$$p \approx \frac{\lambda}{2.4} \text{ for outer ring conductor (in the sub - 6GHz bands)} \quad (53)$$

$$p = 0.41\lambda \text{ for outer ring conductor (in the sub - 6GHz bands)} \quad (54)$$

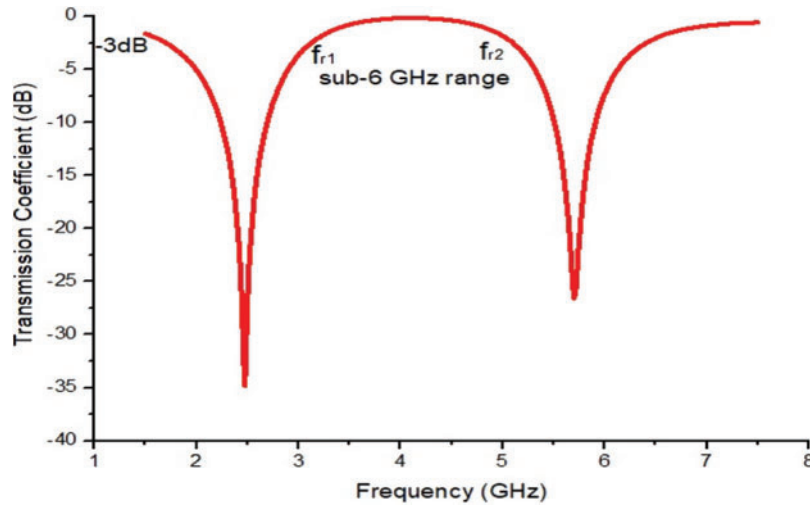


Figure 4: Illustrations of band pass characteristics from the plot of transmission coefficient vs. frequency in sub-6 GHz range

After fixing the value of M and the ring diameters, the effective thickness of both conducting rings is evaluated (i.e., d_1 and d_2 by varying t/λ values) using an Eq. (54) which are mentioned in the Tab. 2 for 3 GHz frequency and in the Tab. 3 for 5 GHz frequency. The percentage deviation is also reported which indicates the difference between the simulated and from a fixed desired value. Further to have more clarity, the graphical illustration is plotted in the Figs. 5 and 6 to have an insight of this design. Also, the inner conductive ring possesses the dimensions at the operating frequency i.e., 5 GHz and at normal angle of incidence, the Eq. (19) reduces to:

$$p < \lambda; p \approx \frac{\lambda}{1.5} \text{ for inner ring conductor (in the sub – 6GHz bands)} \tag{55}$$

Also the expression is reduced from the Eq. (20) for the inner ring in the sub-6 GHz range as:

$$p = 0.66\lambda \text{ for inner ring conductor (in the sub – 6GHz bands)} \tag{56}$$

It should be remembered that the resonant frequency measured in the simulation process is taken at the level where transmission coefficient decreases to -3 dB value. By fixing the value of p , the variations of the characteristics at different values of t/λ is illustrated in the Tabs. 2 and 3.

Table 2: Outer ring parameters for 0° AOI at 3 GHz

Parameters	Values			
t_1/λ_1	0.005	0.015	0.026	0.036
p	$0.55 \lambda_{\text{mid}}$	$0.55 \lambda_{\text{mid}}$	$0.55 \lambda_{\text{mid}}$	$0.55 \lambda_{\text{mid}}$
d_1	$0.20 \lambda_{\text{mid}}$	$0.22 \lambda_{\text{mid}}$	$0.23 \lambda_{\text{mid}}$	$0.24 \lambda_{\text{mid}}$
t_1	$0.0069 \lambda_{\text{mid}}$	$0.020 \lambda_{\text{mid}}$	$0.034 \lambda_{\text{mid}}$	$0.048 \lambda_{\text{mid}}$
f_{r1} (simulated)	3.13 GHz	3.46 GHz	3.72 GHz	3.91 GHz
λ_1	$1.32 \lambda_{\text{mid}}$	$1.32 \lambda_{\text{mid}}$	$1.32 \lambda_{\text{mid}}$	$1.32 \lambda_{\text{mid}}$

(Continued)

Table 2: Continued

Parameters	Values			
% deviation of f_{r1} from 3 GHz	4.3	15.3	24	30

Table 3: Inner ring parameters for 0° AOI at 5 GHz

Parameters	Values			
t_2/λ_2	0.005	0.015	0.026	0.036
p	$0.55 \lambda_{\text{mid}}$	$0.55 \lambda_{\text{mid}}$	$0.55 \lambda_{\text{mid}}$	$0.55 \lambda_{\text{mid}}$
d_3	$0.087 \lambda_{\text{mid}}$	$0.095 \lambda_{\text{mid}}$	$0.104 \lambda_{\text{mid}}$	$0.112 \lambda_{\text{mid}}$
t_2	$0.004 \lambda_{\text{mid}}$	$0.012 \lambda_{\text{mid}}$	$0.021 \lambda_{\text{mid}}$	$0.029 \lambda_{\text{mid}}$
f_{r2} (simulated)	5.30 GHz	5.15 GHz	5.05 GHz	4.83 GHz
λ_2	$0.83 \lambda_{\text{mid}}$	$0.83 \lambda_{\text{mid}}$	$0.83 \lambda_{\text{mid}}$	$0.83 \lambda_{\text{mid}}$
% deviation of f_{r2} from 5 GHz	6	3	1	3.4

A significant outcome of this analysis is that the relative deviation percentage of the resonant frequency from the predicted value is reported for different values of the p by varying the t/λ ratio. It is interpreted from the Figs. 5a and 5b that the resonant frequencies due to both the concentric rings shows the variation at a certain rate in terms of an increase in the transmission bandwidth at a normalized incidence angle (0° in our design) with the variation of t/λ ratio. The effect of the variation of the periodicity is also reported for the proposed design of DCRFSS geometry. As the value of the periodicity is increased, the frequency drift is visualized on both higher and the lower ends. The bandwidth enhancement is reported by the variation of the periodicity as depicted in the Tab. 4 and illustrated in the Fig. 6.

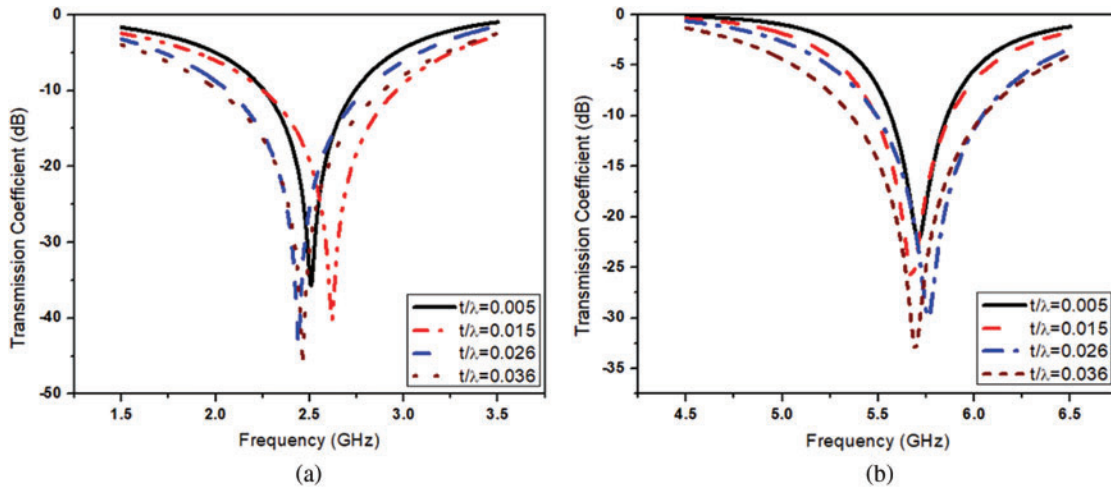


Figure 5: Effect of varying t/λ of the DCRFSS with respect to the resonant frequency for (a) outer conducting ring, (b) inner conducting ring

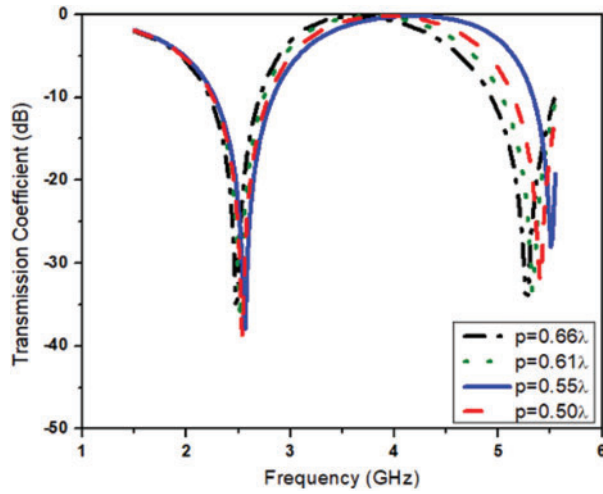


Figure 6: Effect of varying periodicity (p) on the transmission response of the DCRFSS

Table 4: Effect of varying periodicity on the transmission coefficient of the DCRFSS

Parameters	Values			
p	$0.50 \lambda_{\text{mid}}$	$0.55 \lambda_{\text{mid}}$	$0.61 \lambda_{\text{mid}}$	$0.66 \lambda_{\text{mid}}$
f_{r1} (simulated) (GHz)	3.13	2.76	2.75	2.75
% deviation of f_{r1} from 3 GHz	4.3	8	8.33	8.33
f_{r2} (simulated) (GHz)	5.18	5.35	5.39	5.28
% deviation of f_{r2} from 5 GHz	3.6	7	7.8	5.6

The synthesis approach aids in the determination of equivalent circuit characteristics like as inductance and capacitance, as shown in Fig. 3b in the sub-6 GHz FR1 spectrum and listed in Tab. 5.

Table 5: Lumped circuit parameters extracted from ECM

Parameters	Values
f_{r1}	3.13 GHz
f_{r2}	5.18 GHz
p	$0.55 \lambda_{\text{mid}}$
t_1	$0.0069 \lambda_{\text{mid}}$
t_2	$0.013 \lambda_{\text{mid}}$
d_1	$0.207 \lambda_{\text{mid}}$
d_3	$0.09 \lambda_{\text{mid}}$
Input \rightarrow Output	
L_1 Mathematically evaluated	5.385 nH
L_2 Mathematically evaluated	8.624 nH

(Continued)

Table 5: Continued

Parameters	Values
C_2 Mathematically evaluated	0.483 pF
C_3 Mathematically evaluated	0.109 pF

As seen in the DCRFSS frequency response model, the transmission coefficient (S_{21}) reaches a very low level at the two resonant frequencies (f_{r1} and f_{r2}). The resonance frequencies, f_{r1} and f_{r2} , are discussed and are controlled by adjusting the thickness of the outer and inner rings. It can be observed that the outer ring expresses the inner resonant frequency, and the inner ring geometry represents the outer resonant frequency. It is clear from the [Tab. 6](#), that the percentage deviation is less than 1% for the resonant frequencies extracted from the mathematical analysis. The lumped circuit parameters are then entered into the ANSYS circuit editor, and simulation is performed for validating the design by extracting the transmission characteristics.

Table 6: Verification of ECM model by extracting resonant frequencies

Parameters	Values
L_1 (nH) Mathematically evaluated	5.385
L_2 (nH) Mathematically evaluated	8.624
C_2 (pF) Mathematically evaluated	0.483
C_3 (pF) Mathematically evaluated	0.109
Input → Output	
f_{r1} GHz (as per Eq. (1))	3.12
f_{r2} GHz (as per Eq. (2))	5.19
% deviation of first resonant frequency	4
% deviation of second resonant frequency	3.8

[Fig. 7a](#) depicts the circuit diagram of the suggested DCRFSS design, which clearly depicts the operating principle of a two-port network whereas the graphical comparison for the transmission coefficient curves is depicted in the [Fig. 7b](#). The transmission coefficient graphs retrieved from this analysis are in line with the graphs of HFSS simulator which authenticate our design for sub-6 GHz FR1 spectrum. The deviation in the resonant frequency is reported from the results extracted from the two simulation models and is illustrated in the [Tab. 7](#).

It is clearly indicated in the [Tab. 7](#) that the graphs with higher and lower resonant frequencies as retrieved from the two modeling techniques are in line with each other. The percentage deviation is retrieved equal 10 percent for lower resonant frequency and 3.2 percent for the higher resonant frequency. The DCRFSS has the intrinsic quality of having equal output characteristics within a particular range of incidence angle and is also polarization independent, as demonstrated by the study in the [Tabs. 6](#) and [7](#) respectively. The response of transmission coefficient is reported at different polarization angles in the [Fig. 8a](#) and at oblique angles of incidence in the [Fig. 8b](#).

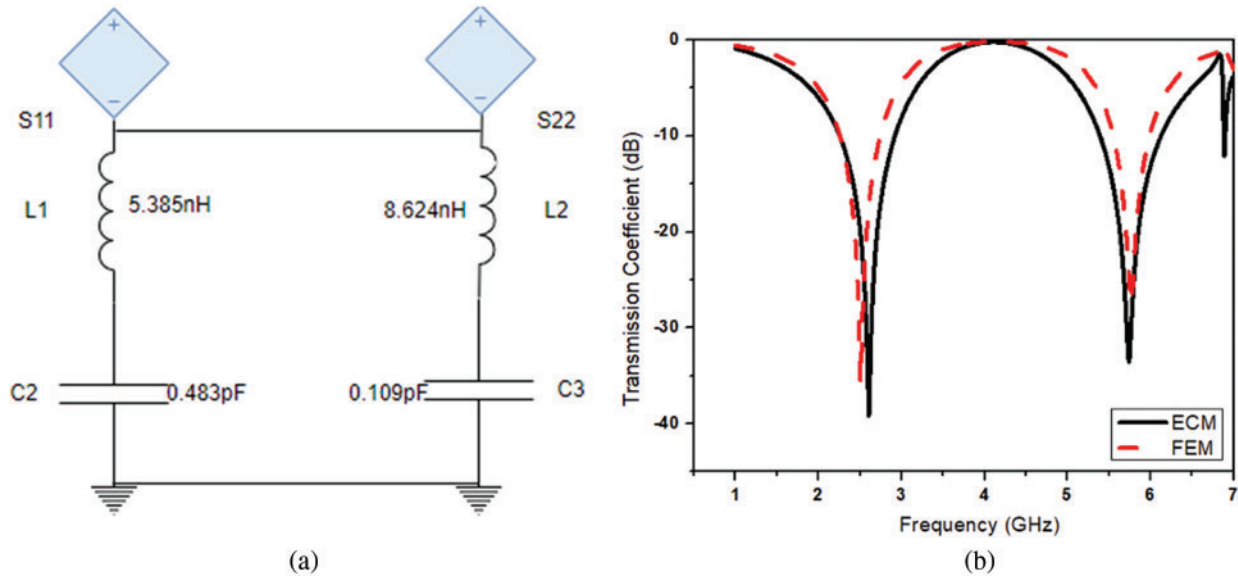


Figure 7: DCRFSS structure (a) circuit schematic, (b) transmission coefficient graphs extracted from HFSS (FEM) and circuit editor (ECM)

Table 7: Comparative analysis of the resonant frequencies retrieved from ECM and FEM techniques

Parameters	Values
f_{r1} (HFSS)	3.13 GHz
f_{r2} (HFSS)	5.18 GHz
FEM vs. ECM	
f_{r1} (Circuit Editor)	3.47 GHz
f_{r2} (Circuit Editor)	5.01 GHz
% deviation in ECM compared to FEM	10
% deviation in ECM compared to FEM	3.2

The polarization conversion ratio (PCR) is an important parameter to be considered while designing the proposed DCRFSS. The values of the transmission and reflection polarization conversion ratios must be identified for reporting of polarization insensitive behavior. In contrast to the traditional metal-ground transmissive polarization converter, the suggested DCRFSS is designed to be incorporated as a superstrate over an antenna, and hence, its reflection coefficient is not zero. Hence, when calculating the values of the transmissive polarization conversion ratio (TPCR), the reflection and transmission ratios of y-to-x and y-to-y polarization conversions should be taken into mind. The term TPCR is expressed in terms of the reflection and the transmission ratios as shown:

$$TPCR = \frac{|t_{xy}|^2}{(|r_{xy}|^2 + |r_{yy}|^2 + |t_{xy}|^2 + |t_{yy}|^2)} \quad (57)$$

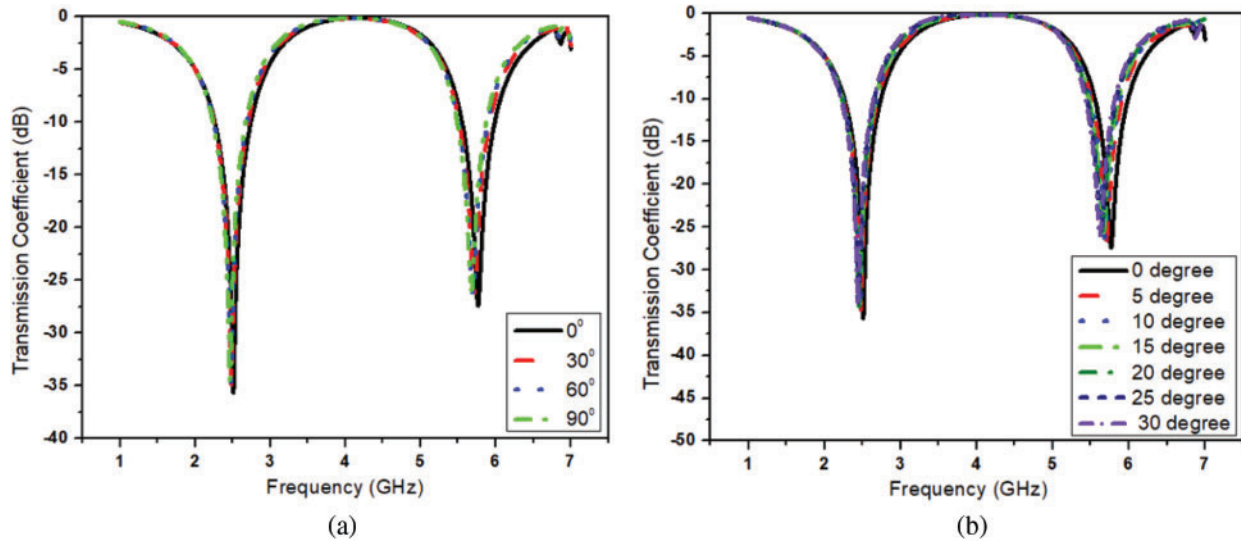


Figure 8: Transmission response of the DCRFSS (a) at polarization angles, (b) at oblique AOI's

The value of TPCR is above 96% for the entire frequency spectrum within the desired operating band. Also, the values reported in the Tab. 8 clearly indicate that the designed DCRFSS is polarization insensitive as the resonant frequencies attains the same value for different angle ' ϕ ' ranging from 0° to 90° . As illustrated in Fig. 8b, the intended structure of DCRFSS is synthesized for various oblique incidence angles. The limit of AOI for this design to operate is up to 30° for satisfying the Eq. (20) as given below:

$$p(1 + \sin 30) < \frac{\lambda}{\sqrt{\epsilon_{\text{eff}}}} \quad (58)$$

Table 8: Response of DCRFSS as a band pass filter at different polarization angles

Parameters	Values			
Angle (ϕ) (degree)	0°	30°	60°	90°
f_{r1} (GHz)	3.13	3.07	3.05	3.03
f_{r2} (GHz)	5.18	5.16	5.16	5.15
Bandwidth (MHz)	2050	2090	2110	2120
% Fractional Bandwidth (FBW)	49.33	50.78	51.40	51.83
Transmission polarization conversion rate (TPCR) (%)	0	98	97	96.69

The average bandwidth is essentially unaffected by angle fluctuation, and for high incidence angles such as 30° , the structure retains appropriate performance, as shown in Tab. 9.

As shown in Figs. 8a and 8b, the graphs virtually correspond with each other, making this design stable in terms of polarization and AOI by presenting same features up to 30° of incident angles and 90° for the polarization angles.

Table 9: Band-pass response of DCRFSS at different oblique incident angles

Parameters	Values						
Angle (ϕ) (degree)	0°	5°	10°	15°	20°	25°	30°
f_{r1} (GHz)	3.13	3.07	3.05	3.02	3.00	2.99	2.97
f_{r2} (GHz)	5.18	5.16	5.15	5.14	5.14	5.13	5.12
Bandwidth (MHz)	2050	2090	2100	2120	2140	2140	2150
% FBW	49.33	50.78	51.21	51.96	52.57	52.70	53.21
% deviation of f_{r1} from 3.13 GHz	0	1.9	2.5	3.5	4.1	4.4	5.1
% deviation of f_{r2} from 5.18 GHz	0	0.38	0.57	0.77	0.77	0.96	1.15

4 Array Modeling and Experimental Set-up

According to Floquet theory, the frequency selective surfaces have identical characteristics in when extended to an array made by combinations of a unit cell [39]. The dimensions of the unit cell are duplicated for all array items. Using this theory, the analysis was extended to create a 2×2 DCRFSS array that can be generalized into an $N \times N$ array. The designed prototype is illustrated in the Fig. 9a. A unique DCRFSS schematic is utilized to create a prototype with the needed properties. This DCRFSS is constructed utilizing a straight-forward design of single surface layers. At sub-6 GHz frequency ranges of operation, the structure has a low insertion loss. The prototype's frequency response is evaluated for both normal incidence and oblique incidence angles. The measuring investigation is completed by putting together an experimental setup, as shown in Fig. 9b and the measurement set-up in an anechoic chamber for reporting the design characteristics is illustrated in the Fig. 9c. The retrieved measurement findings under the free space environment circumstances are compared with the simulated ones, in the Fig. 9d.

The proposed DCRFSS design's benefits are compared to the state-of-the-art literature as illustrated in the Tab. 10. The comparison is based on design factors such as substrate thickness, size, and dielectric constant, as well as bandwidth performance. The proposed design in this publication has demonstrated very excellent bandwidth with an ultra-thin design.

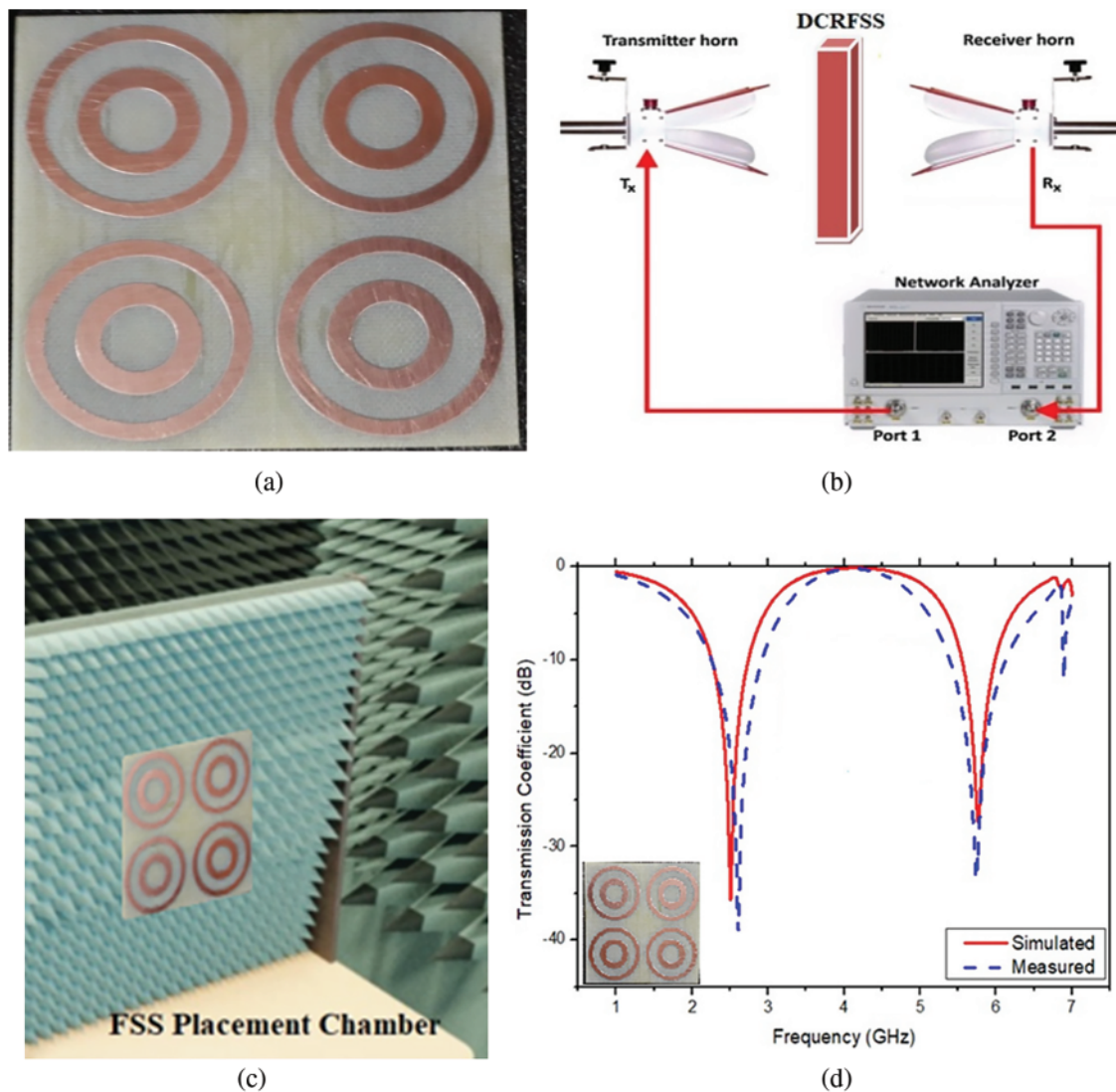


Figure 9: Illustration of the DCRFSS (a) fabricated prototype, (b) experimental set up, (c) 2×2 DCRFSS placed in an anechoic chamber, (d) comparative analysis of simulated and measured S-parameters

Table 10: State of art comparison of the proposed DCRFSS

Cited work	Substrate thickness	Cell size	ϵ_r	-10 dB FBW (%)	Elements used	Remarks
[9]	—	$0.175\lambda \times 0.175\lambda$	2.1	37	Double square and cross loops (DSCL)	Limited bandwidth

(Continued)

Table 10: Continued

Cited work	Substrate thickness	Cell size	ϵ_r	-10 dB FBW (%)	Elements used	Remarks
[10]	0.046 λ	0.18 λ \times 0.18 λ	2.2	34	Double square with gridded loops	Includes high structural complexity
[11]	0.003 λ	0.26 λ \times 0.26 λ	3.5	46	Modified DSL	Not suited for large power applications
[15]	0.13 λ	1.67 λ \times 1.67 λ	4.4	32.5	Square loop with grids	Substantial thickness of substrate
[42]	0.01 λ	Not specified	2.2	46	Tunable Meta surfaces	Angular stability not studied
[43]	0.06 λ	0.2 λ \times 0.2 λ	2.2	24	Jerusalem cross surface	Limited bandwidth
Proposed work	0.022 λ	0.20 λ – outer loop 0.09 λ – inner loop	4.4	49.33	Double Concentric Ring structure	Wide bandwidth with angular and polarization stability

5 Conclusion

A unique numerical synthesis approach for creating a simple, miniaturize, and a broadband FSS that may be employed in the construction of microwave spatial filters in the sub-6 GHz FR1 frequency region is described. Spatial filters are created using double concentric ring frequency selective surface structures, which have high bandwidth and polarization independence. For the estimate of physical dimensions, a unique numerical synthesis approach is suggested. The effect of the variation of periodicity, loop diameters, polarization angles and incident angles with respect to wavelength is analyzed in this study. The prototype is used to validate the synthesis of the proposed structure. In addition, an analogous circuit analysis is offered for examining the intended work in terms of its electrical behavior to demonstrate the filtering process. The suggested structure is polarization insensitive, with a steady transmission response at incidence angles spanning from 0° to 30°. The suggested spatial filters based on the concentric ring design of the FSS proves to be a viable option to be placed as a superstrate with the antenna in sub-6 GHz 5G applications for improving the radiation characteristics.

Funding Statement: Authors have received no specific funding for completing this study.

Conflicts of Interest: Authors hereby declare that they have no conflicts of interest to report regarding the present study.

References

- [1] A. Kapoor, R. Mishra and P. Kumar, "Frequency selective surfaces as spatial filters: Fundamentals, analysis and applications," *Alexandria Engineering Journal*, vol. 61, no. 6, pp. 4263–4293, 2022.
- [2] A. Kapoor, P. Kumar and R. Mishra, "Analysis and design of a passive spatial filter for sub-6 GHz 5G communication systems," *Journal of Computational Electronics*, vol. 20, no. 5, pp. 1900–1915, 2021.
- [3] A. Jamal, I. Bin, Z. Zakaria, B. H. Ahmad, N. Azwan *et al.*, "High gain of UWB planar antenna utilizing FSS reflector for UWB applications," *Computers, Materials & Continua*, vol. 70, no. 1, pp. 1419–1436, 2022.
- [4] A. Kapoor, R. Mishra and P. Kumar, "A compact high gain printed antenna with frequency selective surface for 5G wideband applications," *Advanced Electromagnetics*, vol. 10, no. 2, pp. 27–38, 2021.

- [5] A. Kapoor, R. Mishra and P. Kumar, "Complementary frequency selective surface pair-based intelligent spatial filters for 5G wireless systems," *Journal of Intelligent Systems*, vol. 30, no. 1, pp. 1054–1069, 2021.
- [6] S. Habib, G. I. Kiani, M. Fasih, S. M. Abbas, A. J. Aljohani *et al.*, "Ultra-wideband frequency selective surface for communication applications," *Computers, Materials & Continua*, vol. 70, no. 3, pp. 6177–6187, 2022.
- [7] N. S. Ishak, F. C. Seman, N. Zainal and N. A. Awang, "Detection of low sugar concentration solution using frequency selective surface (FSS)," *CMC-Computers, Materials & Continua*, vol. 71, no. 2, pp. 2869–2882, 2022.
- [8] A. Kapoor, R. Mishra and P. Kumar, "Novel wideband frequency selective surface based spatial filters for sub-6 GHz 5G devices," *2021 4th Biennial International Conference on Nascent Technologies in Engineering (ICNTE)*, pp. 1–6, 2021.
- [9] D. Li, T. Li, E. Li and Y. Zhang, "A 2.5-D angularly stable frequency selective surface using via-based structure for 5G EMI shielding," *IEEE Transactions on Electromagnetic Compatibility*, vol. 60, no. 3, pp. 768–775, 2018.
- [10] A. Kapoor, R. Mishra and P. Kumar, "Slotted wideband frequency selective reflectors for sub-6 GHz 5G devices," *2021 International Conference on Computing, Communication, and Intelligent Systems (ICCCIS)*, pp. 786–791, 2021.
- [11] R. Sivasamy, L. Murugasamy, M. Kanagasabai, E. F. Sundarsingh and M. GulamNabiAlsath, "A low profile paper substrate based dual band FSS for GSM shielding," *IEEE Transactions on Electromagnetic Compatibility*, vol. 58, no. 2, pp. 611–614, 2016.
- [12] R. J. Langley and E. A. Parker, "Equivalent circuit model for arrays of square loops," *Electron Letters*, vol. 18, no. 7, pp. 294–296, 1982.
- [13] T. Li, D. Li, L. Zhou and E. Li, "Miniaturized FSS structure with excellent angular stability based on strong coupling for millimeter-wave communication," *Electronic Letters*, vol. 54, no. 8, pp. 511–513, 2018.
- [14] D. Ferreira, R. F. S. Caldeirinha, I. Cuinas and T. R. Fernandes, "Square loop and slot frequency selective surfaces study for equivalent circuit model optimization," *IEEE Transactions on Antennas and Propagation*, vol. 63, no. 9, pp. 3947–3955, 2015.
- [15] B. S. da Silva, A. L. P. S. Campos and A. G. Neto, "Narrowband shielding against electromagnetic interference in LTE 4G systems using complementary frequency selective surfaces," *Microwave Optical Technology Letters*, vol. 60, no. 9, pp. 2293–2298, 2018.
- [16] S. Keyrouz, G. Perotto and H. J. Visser, "Frequency selective surface for radio frequency energy harvesting applications," *IET Microwave, Antennas Propagation*, vol. 8, no. 7, pp. 523–531, 2014.
- [17] D. Ferreira, R. F. S. Caldeirinha, I. Cuinas and T. R. Fernandes, "Square loop and slot frequency selective surfaces study for equivalent circuit model optimization," *IEEE Transactions on Antennas and Propagation*, vol. 63, no. 9, pp. 3947–3955, 2015.
- [18] V. K. Kanth and S. Raghavan, "Complementary frequency selective surface array optimization using equivalent circuit model," *2017 IEEE MTT-S International Microwave and RF Conference (IMaRC)*, pp. 1–4, 2017.
- [19] B. S. da Silva, A. L. P. S. Campos and A. G. Neto, "Equivalent circuit model for analysis of frequency selective surfaces with ring and double concentric ring apertures," *IET Microwaves, Antennas & Propagation*, vol. 14, no. 7, pp. 600–607, 2020.
- [20] M. B. Perotoni, L. A. D. Andrade and C. Junqueira, "Design, prototyping and measurement of a cascaded 6-GHz frequency selective surface array," *Journal of Aerospace Technology and Management*, vol. 8, no. 2, pp. 137–142, 2016.
- [21] R. Anwar, L. Mao and H. Ning, "Frequency selective surfaces: A review," *Applied Sciences*, vol. 8, no. 9, pp. 1689, 2018.
- [22] G. Bharti, G. Singh, K. R. Jha and R. Jyoti, "Circular ring frequency selective surface: A novel synthesis technique," *2013 Sixth International Conference on Contemporary Computing (IC3)*, pp. 491–496, 2013.

- [23] V. K. Kanth and S. Raghavan, "Design and optimization of complementary frequency selective surface using equivalent circuit model for wideband EMI shielding," *Journal of Electromagnetic Waves and Applications*, vol. 34, no. 1, pp. 51–69, 2020.
- [24] W. Mohyuddin, D. Kim, H. Choi and K. Kim, "Comparative study of square and circular loop frequency selective surfaces for millimeter-wave imaging diagnostics systems," *Sensors*, vol. 18, no. 9, pp. 3079, 2018.
- [25] S. Habib, G. I. Kiani and M. F. U. Butt, "A convoluted frequency selective surface for wideband communication applications," *IEEE Access*, vol. 7, pp. 65075–65082, 2019.
- [26] V. K. Kanth and S. Raghavan, "Ultrathin wideband slot and patch FSS elements with sharp band edge characteristics," *International Journal of Electronics*, vol. 107, no. 9, pp. 1365–1385, 2020.
- [27] M. ZahirJoozdani and M. Khalaj Amirhosseini, "Equivalent circuit model for the frequency selective surface embedded in a layer with constant conductivity," *IEEE Transactions on Antennas and Propagation*, vol. 65, no. 2, pp. 705–712, 2017.
- [28] S. Lee, G. Zarrillo and C. L. Law, "Simple formulas for transmission through periodic metal grids or plates," *IEEE Transactions Antennas Propagation*, vol. 30, no. 5, pp. 904–909, 1982.
- [29] N. Liu, X. Sheng, C. Zhang, J. Fan and D. Guo, "A design method for synthesizing wideband band-stop FSS via its equivalent circuit model," *IEEE Antennas and Wireless Propagation Letters*, vol. 16, pp. 2721–2725, 2017.
- [30] A. Kapoor, R. Mishra and P. Kumar, "Compact wideband-printed antenna for sub-6-GHz fifth-generation applications," *International Journal of Smart Sensing and Intelligent Systems*, vol. 13, no. 1, pp. 1–10, 2020.
- [31] J. Lee, E. Tejedor, K. Ranta-aho, H. Wang, K. T. Lee *et al.*, "Spectrum for 5G: Global status, challenges, and enabling technologies," *IEEE Communication Magazine*, vol. 56, no. 3, pp. 12–18, 2018.
- [32] I. S. Masoodi, I. Ishteyaq and K. Muzaffar, "Extra compact two element sub-6 GHz MIMO antenna for future 5G wireless applications," *Progress In Electromagnetics Research Letters*, vol. 102, pp. 37–45, 2022.
- [33] M. Shobana, R. Pandeewari and S. Raghavan, "Design of sub-6 GHz antenna using negative permittivity metamaterial for 5G applications," *International Journal of Systems Assurance Engineering and Management*, vol. 88, no. 16, pp. 113, 2022.
- [34] N. Marcuvitz, *Waveguide Handbook*, 1st ed., New York: McGraw-Hill, 1951.
- [35] K. Sarabandi and N. Behdad, "A frequency selective surface with miniaturized elements," *IEEE Transactions on Antennas and Propagation*, vol. 55, no. 5, pp. 1239–1245, 2007.
- [36] R. J. Langley and A. J. Drinkwater, "Improved empirical model for the Jerusalem cross," *IEE Proceedings Microwaves, Optics and Antennas*, vol. 129, no. 1, pp. 1–6, 1982.
- [37] R. J. Langley and E. A. Parker, "Double-square frequency-selective surfaces and their equivalent circuit," *Electronics Letters*, vol. 19, no. 17, pp. 675–677, 1983.
- [38] X. Yao, M. Bai and J. Miao, "Equivalent circuit method for analyzing frequency selective surface with ring patch in oblique angles of incidence," *IEEE Antennas and Wireless Propagation Letters*, vol. 10, pp. 820–823, 2011.
- [39] N. Amitay and V. Galindo, "On the scalar product of certain circular and Cartesian wave functions," *IEEE Transaction. Microwave Theory and Technology*, vol. 16, no. 4, pp. 265–266, 1968.
- [40] R. Agarwal, M. Bohner, A. Domoshnitsky and Y. Goltser, "Floquet theory and stability of nonlinear integro-differential equations," *Acta Mathematica Hungarica*, vol. 109, no. 4, pp. 305–330, 2005.
- [41] C. C. Chen, "Scattering by a two-dimensional periodic array of conducting plates," *IEEE Transactions on Antennas and Propagation*, vol. 18, no. 5, pp. 660–665, 1970.
- [42] M. M. Masud, B. Ijaz, I. Ullah and B. Braaten, "A compact dual band EMI meta-surface shield with an actively tunable polarized lower band," *IEEE Transactions on Electromagnetic Compatibility*, vol. 54, no. 5, pp. 1182–1185, 2012.
- [43] L. B. Wang, K. Y. See, J. W. Zhang, B. Salam and A. C. W. Lu, "Ultrathin and flexible screen-printed meta-surfaces for EMI shielding applications," *IEEE Transactions on Electromagnetic Compatibility*, vol. 53, no. 3, pp. 700–705, 2011.